ChemPlusChem

Research Article
doi.org/10.1002/cplu.202400311

Chemistry Europe
European Chemical Societies Publishing

www.chempluschem.org

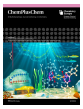

Introducing the Bis(mesitoyl)phosphide Ligand into Dinuclear Trivalent Rare Earth Metal Coordination Chemistry

Saroshan Deshapriya,[a] Francis Delano IV,[a] and Selvan Demir*[a]

Anionic ancillary ligands play a critical role in the construction of rare earth (RE) metal complexes due to the large influence on the stability of the molecule and engendering emergent electronic properties that are of interest in a plethora of applications. Supporting ligands comprising oxygen donor atoms are highly pursued in RE chemistry owing to the high oxophilicity innate to these ions. The scarcely employed bis(acyl)phosphide (BAP) ligands feature oxygen coordination sites and contain a phosphide backbone rendering it attractive for RE-coordination chemistry. Here, we integrate bis(mesitoyl)phosphide (^{mes}BAP) as an ancillary ligand into RE^{III} chemistry to generate the first dinuclear trivalent RE complexes containing BAP ligands; [{^{mes}BAP}$_2$RE(THF)(μ-Cl)]$_2$ (RE=Y, (**1**), Gd (**2**), and Dy (**3**); THF = tetrahydrofuran). Each RE center is ligated to two monoanionic ^{mes}BAP ligands, one THF molecule and one chloride ion. All three molecules were characterized through single-crystal X-ray diffraction, ^{31}P NMR, IR and UV-Vis spectroscopy. ^{31}P, ^{1}H and ^{13}C NMR on the diamagnetic yttrium congener **1** confirm asymmetric ligand coordination. DFT calculations conducted on **2** provided insight into the electronic structure. The magnetic properties of **2** and **3** were investigated via SQUID magnetometry. The Gd^{III} ions exhibit weak antiferromagnetic coupling, corroborated by DFT results.

Introduction

The unusual geometries and electronic properties of the rare earth (RE) metal ions necessitates judicious ancillary ligand design.[1–3] Typically, ancillary ligands suitable for the pursuit of new RE-based materials have several key attributes: hard anionic charges, multiple coordination sites, and sterically encumbering substituents to saturate the metal ion. The development of new ligand architectures is essential to the field of RE chemistry as appropriate metal-ligand pairing affects the electronic and physical properties of the metal center. Deliberate tailoring of the crystal field has led to otherwise unprecedented reactivity,[4–6] luminescent properties,[7,8] and magnetic behavior.[9–11]

Owing to the oxophilicity exhibited by RE^{III} ions, anionic ligands featuring oxygen binding sites have found prolific use.[12–14] Among those, β-diketone ligands such as substituted acetylacetonates (acac) have been used extensively owing to the facile availability, and ease of substitution.[15–17]

In contrast, the phosphorus analog of acac, bis(acyl)phosphides (BAP) are significantly underutilized ligands in coordination chemistry. Similar to acac, BAP ligands are chelating and tunable, but offer several additional advantages. Firstly, inclusion of a phosphorus atom into the ligands backbone introduces an additional chelation site to interact with softer metals, which can be an intriguing way to isolate heteromultimetallic systems.[18,19] Secondly, the presence of a P atom in the BAP ligand scaffold grants the ability to monitor a chemical reaction involving the paramagnetic RE metals via ^{31}P NMR spectroscopy owing to the longer relaxation times typically exhibited by ^{31}P nuclei relative to ^{1}H.[20]

Despite their advantages, the coordination chemistry of BAP ligands with *f*-elements is underexplored. The scarcity of BAP chemistry may be attributed to the more elaborate synthesis relative to more classical diketones,[21] but the compelling advantages renders the use of this ligand class attractive. Hence, recently, the first reports of *f*-element compounds containing BAP ligands appeared which are composed of mononuclear complexes of U^{III},[22] U^{IV},[23] Eu^{III} and Eu^{II}.[24] In all cases, the central metal ion is ligated by three anionic BAP chelates, thus saturating the coordination sphere of the metal ion, Figure 1. Very recently, a Eu^{II} BAP dimer has been reported.[25] Notably, there are no dinuclear or even higher nuclearity BAP *f*-element compounds known, employing actinides or trivalent RE metals

The generation of large multi-metallic molecular compounds with metal ions connected through organic bridging ligands are of paramount interest, as the attributes of several metal centers can be used in harmony, leading to unique catalytic,[26,27] and electronic properties[28,29]. For the successful synthesis of such molecules, judiciously selected molecular building blocks bearing ancillary ligands must be in place. Halide-bridged dinuclear complexes constitute a favorable

[a] S. Deshapriya, F. Delano IV, S. Demir
Department of Chemistry, Michigan State University, 578 S. Shaw Lane, East Lansing, Michigan 48824, USA
E-mail: sdemir@chemistry.msu.edu

Supporting information for this article is available on the WWW under https://doi.org/10.1002/cplu.202400311

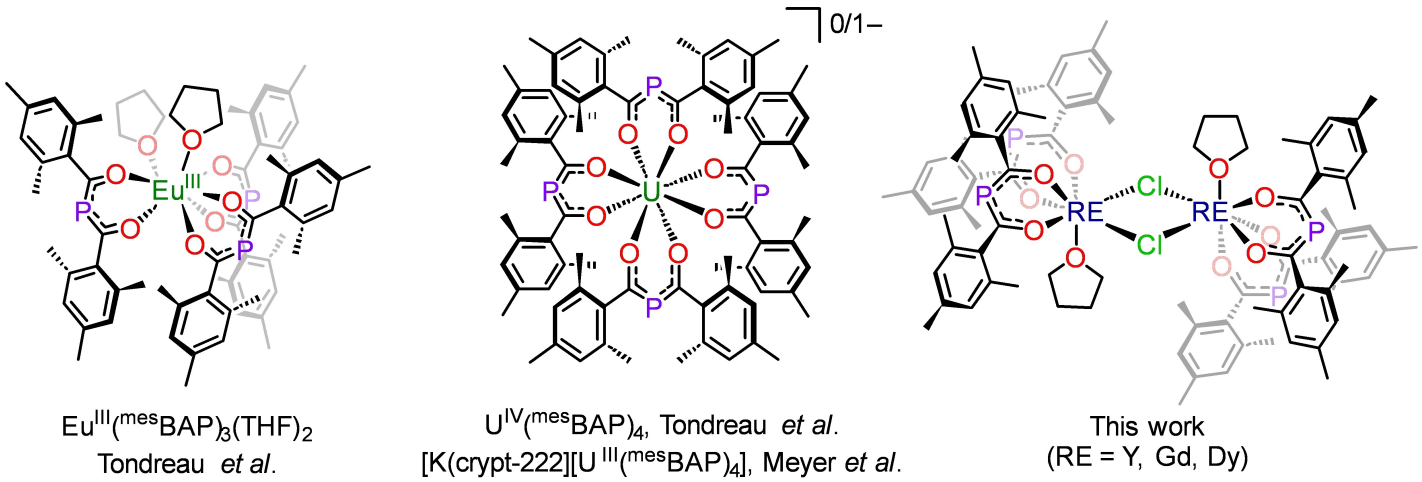

Figure 1. Known ^{mes}BAP complexes with *f*-block metals.

starting point, which can be subsequently reacted with neutral organic ligands. The utility of this approach was recently reported with systems composed of guanidinate ligands by some of us.[30]

Here, the synthesis and characterization of the first dinuclear trivalent RE complexes bearing mesitoyl-substituted BAP ligands is presented. The three bimetallic RE complexes [{^{mes}BAP}$_2$RE(THF)(μ-Cl)]$_2$ (RE=Y (**1**), Dy (**2**), and Gd (**3**); ^{mes}BAP = bis(2,4,6-trimethylbenzoyl)phosphide; THF = tetrahydrofuran) were isolated and unambiguously characterized through single-crystal X-ray diffraction analysis, ^{31}P NMR spectroscopy, electronic absorption spectroscopy and SQUID magnetometry. The diamagnetic nature of the Y^{III} ions in **1** enabled additional characterization via ^{1}H and ^{13}C NMR spectroscopy. The isotropic nature of the Gd^{III} ions in **2** allowed Density Functional Theory (DFT) analysis of the electronic structure. In sum, these compounds feature the first dinuclear trivalent rare earth metal complexes featuring a BAP ligand scaffold.

Results and Discussion

The bis(2,4,6-trimethylbenzoyl)phosphide (^{mes}BAP) chloride-bridged dinuclear rare earth complexes [{^{mes}BAP}$_2$RE(THF)(μ-Cl)]$_2$ (RE=Y (**1**), Gd (**2**), and Dy (**3**); THF = tetrahydrofuran) were synthesized through a stoichiometric salt metathesis reaction between two equiv. of the respective rare earth trichlorides, $RECl_3$, and four equiv. of the potassium salt, K[^{mes}BAP],[21] Scheme 1. Storage of concentrated toluene solutions at −35 °C for two days yielded plate-shaped crystals of [{^{mes}BAP}$_2$RE-(THF)(μ-Cl)]$_2$ in 51%, 52% and 44% crystalline yields, for **1**, **2**, and **3**, respectively. **1** formed light-yellow crystals, while **2** and **3** produced yellow-orange crystals. Complexes **1** and **2** are isostructural and crystallize in the $P2_1/c$ space group with four co-crystallized toluene molecules in the unit cell. Complex **3** crystallizes in $P\bar{1}$ space group with four co-crystallizing toluene molecules, Figures S5 and S9.

Each rare earth metal center is seven-coordinate, and is ligated by two ^{mes}BAP ligands, one THF solvent molecule, and two chloride ligands which are μ-bridging to the other metal ion. The asymmetric unit comprises one RE center coordinated

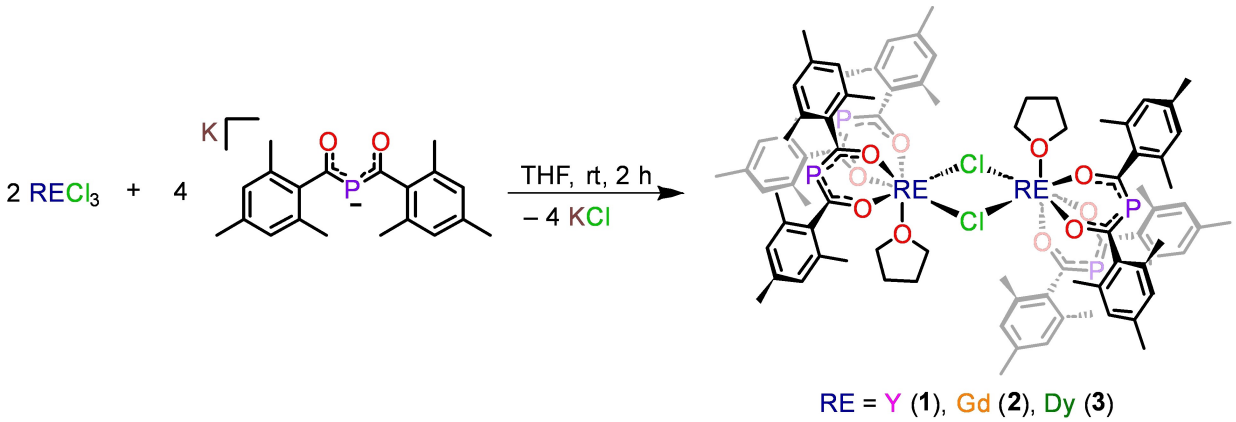

Scheme 1. Synthesis of [{^{mes}BAP}$_2$RE(THF)(μ-Cl)]$_2$ (RE=Y, (**1**), Gd (**2**), and Dy (**3**); THF = tetrahydrofuran; ^{mes}BAP = bis(2,4,6-trimethylbenzoyl)phosphide).

with one Cl, one THF, and two ^{mes}BAP ligands. Thus, each metal center adopts a capped trigonal prismatic geometry, Figure 2. The O–RE–O bite angles arising from the oxygen coordination sites of each κ^2–O,O′-coordinated ^{mes}BAP ligands amount to 74.1(7)° and 75.8(7)° (**1**); 73.5(9)° and 74.7(9)° (**2**); and 75.2(2)° and 75.5(2)° (**3**), respectively. The unequal bite angles indicate an asymmetric coordination of the ligands to the metal centers. An asymmetric coordination of BAP ligands occurs also in the mononuclear europium complex Eu(^{mes}BAP)$_3$(THF)$_2$ where the bite angles span from 70.9(8)°–72.6(7)°.[24] The RE–O_{BAP} bond distances range from 2.227(2)–2.297(2) Å (**1**), 2.266(3)–2.325(2) Å (**2**), and 2.246(4)–2.285(4) Å (**3**) which are similar to RE–O distances in dinuclear complexes bearing oxygen chelates such as acac ligands (e.g. hexafluoroacetylacetonate).[31] Interestingly, the RE–O_{BAP} interatomic distances are shorter relative to the RE–O_{THF} distances, which may be attributed to a stronger metal-ligand interaction due to the negatively charged ^{mes}BAP ligands as opposed to the neutral solvent molecules.

The four-membered {RE_2Cl_2} core of **1**, **2**, and **3** allows for a comparison of distances and angles to other halide-bridged dinuclear compounds. Chloride-bridged dinuclear guanidinate complexes, [{(SiMe$_3$)$_2$NC(N^{i}Pr)$_2$}$_2$RE(μ–Cl)]$_2$,[32–34] are suitable for comparison and feature for RE═Y, Gd, and Dy, RE···RE distances of 4.278(7) Å, 4.356(9) Å, and RE–Cl–RE angles of 103.7(5)°–104.0(5)°, 103.7(9)°–104.1(9)°, and 102.7(6)°. Comparisons can also be drawn to a dinuclear Gd complex consisting of ancillary cyclopentadienyl (Cp) ligands where Cp is a prevalent entity in organometallic chemistry of the lanthanides. Accordingly, the Gd complex, [Cp$_2$Gd(THF)(μ-Cl)]$_2$, exhibits a Gd···Gd distance of 4.455(8) Å and Gd–Cl–Gd angles of 106.6(9)° and 106.7(8)°.[35]

In all cases, both the RE–Cl–RE angles and RE···RE interatomic distances are significantly longer than those observed in **1**, **2**, and **3**, likely a result of the steric hindrance arising from the ligated bulky ^{mes}BAP and the coordinating THF solvent molecules.

The interatomic distances of the ^{mes}BAP ligands reveal information about the bonding nature within the ^{mes}BAP ligand. The O–C distances fall within the range of 1.243(4)–1.265(4) Å, which are in between a C–O distance ascribed to a single and a double bond.[36] Similarly, the C–P distances vary from 1.772(3)–1.796(3) Å, corresponding to an intermediate between a C–P single and a double bond. These bond distances are evidence for the resonance arising from the delocalization of the negative charge within the {OCPCO} moiety of the ^{mes}BAP ligands. A comparison of the bond distances and angles arising from the ^{mes}BAP coordination to the RE centers in **1**, **2**, and **3**, uncovers the largest range for the distances and angles in **1**, suggestive of more asymmetric phosphide coordination.

Spectroscopic Characterization

The paramagnetic nature of the Dy^{III} and Gd^{III} centers in **2** and **3** render meaningful information from ^{1}H and ^{13}C NMR spectroscopy inaccessible. However, the comparatively longer relaxation times shown by ^{31}P nuclei, make the use of ^{31}P NMR

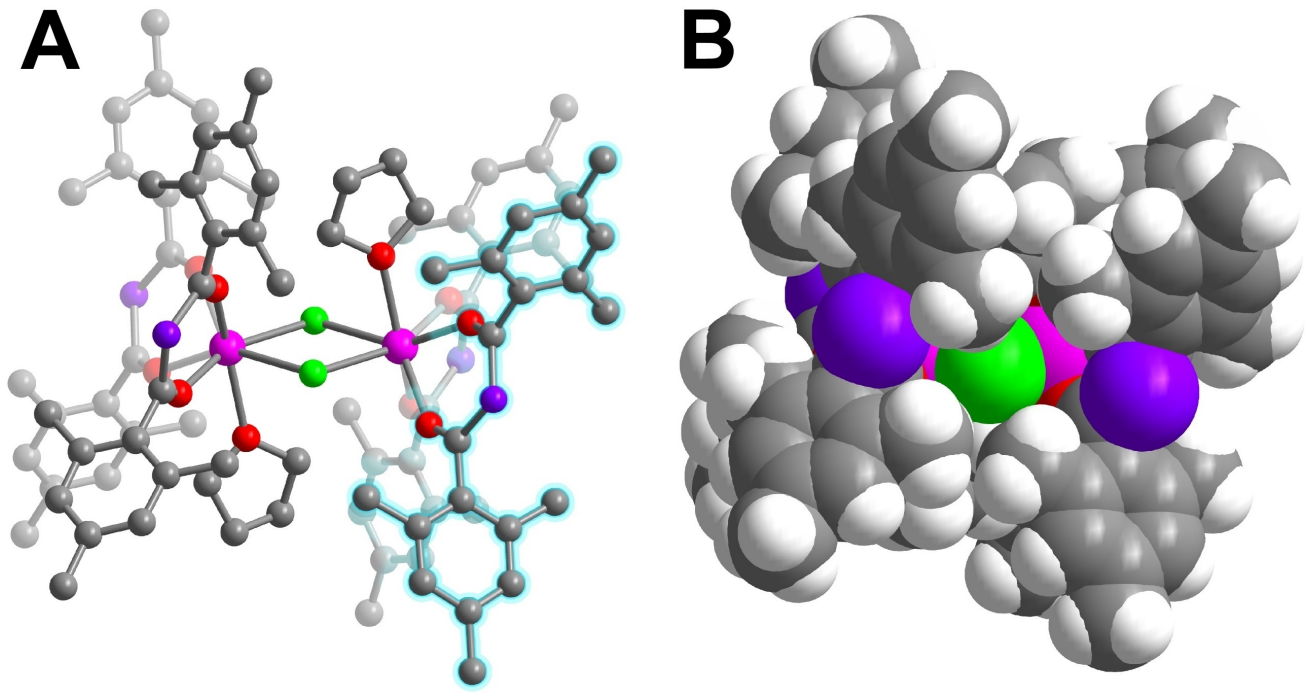

Figure 2. (**A**) Structure of **1** in a crystal of [{^{mes}BAP}$_2$RE(THF)(μ-Cl)]$_2$·4 C_7H_8. Pink, red, purple, green, and gray spheres represent Y, O, P, Cl and C atoms, respectively. H atoms and co-crystallized toluene molecules are omitted. One ^{mes}BAP ligand is highlighted for clearer visibility. (**B**) Space filling model of **1**. Complexes **1**, **2**, and **3** are topologically similar with an inversion center between the RE metals. Selected interatomic distances (Å) and angles (°) for **1**, **2**, and **3**, respectively: RE–O_{BAP} = 2.227(2)–2.297(2), 2.266(3)–2.325(2), 2.246(4)–2.285(4); RE–O_{THF} = 2.392(2), 2.429(2), 2.411(3); RE–Cl = 2.698(8) and 2.779(6), 2.733(1) and 2.812(8), 2.733(2) and 2.740(2); RE···P = 4.124(1) and 4.131(1), 4.160(1) and 4.169(1), 4.085(2) and 4.101(2); RE···RE = 4.273(4), 4.314(4), 4.211(4); C–P–C = 101.3(1)° and 102.3(1)°, 101.6(2)° and 102.5(2)°, 101.1(3)° and 101.5(3)°; RE–Cl–RE = 102.5(2)°, 102.2(3)°, 100.6(4).

spectroscopy attractive with which the chemical shift of the P atoms in the uncoordinated and coordinated ^{mes}BAP ligands can be evaluated, Figures S14–S17.

The ^{31}P chemical shift was referenced to a dilute phosphoric acid solution for all performed ^{31}P NMR studies. The potassium salt of the ^{mes}BAP ligand shows a single ^{31}P peak at 82.45 ppm (H_3PO_4 = 1.55 ppm), Figure S17, which can be used to track changes in the chemical environment of the P atom in ^{mes}BAP. Two peaks are observed at 100.3 ppm and 100.7 ppm for **1**, whereas one signal is monitored for **3** at 91.6 ppm, Figures S14 and S16. This downfield shift relative to the free ligand is attributed to the ligation to the highly Lewis-acidic RE center resulting in significant deshielding of the ^{31}P nucleus. The presence of two resonance peaks for ^{31}P in **1** can be ascribed to the higher degree of asymmetry in coordination observed for complex **1** relative to **2** and **3**. The peak positions resemble known ^{31}P peaks for BAP ligands of RE complexes.[24]

Intriguingly, the ^{31}P NMR spectrum of [{^{mes}BAP}$_2$Gd(THF)(μ-Cl)]$_2$, **2**, lacks signals originating from the phosphide ligands. Even increasing the relaxation delay during acquisition precluded the occurrence of a ^{31}P resonance peak. This is explained due to the enhanced nuclear relaxation times engendered by the presence of the Gd^{III} ion.[37] The ^{31}P NMR spectra for compounds **1**–**3** and ^{1}H and ^{13}C NMR spectra for **1** are provided in Figures S10–S13.

UV-Vis absorption spectroscopy was employed to probe the electronic transitions occurring in **1**, **2**, and **3**. The absorption spectra were collected from 220–1000 nm in THF solutions with concentrations of 10 μM. The electronic absorption spectra for all three compounds resemble closely each other with two major absorption bands centered at 4.71×10^4 cm^{-1} (212 nm), and 2.52×10^4 cm^{-1} (397 nm), Figures 3 and S21.

Both compounds display their maximum absorbances in the UV region of the spectrum. This is similar to the most intense peak positioned at 2.53×10^4 cm^{-1} (396 nm) for the [(^{mes}BAP)$_3$(THF)$_2$] complex, which is assigned to a $\pi\rightarrow\pi^*$ electronic transition of the ^{mes}BAP ligands.[35] The second most intense peak for both **2** and **3** is absorbing in the violet color range of the visible region. This is consistent with the observed bright yellow color of the compounds in solution. To assign electronic excitation transitions to the experimentally observed absorption bands of the electronic absorption spectrum of **2**, time-dependent DFT (TD-DFT) calculations were carried out on the geometry optimized coordinates employing the flipspin function considering 500 excited states. An implicit CPCM solvent model defined for THF was employed for this calculation to match the experimental conditions.

The calculated transitions agree well with the experimentally observed spectra, Figure 3. The most intense transitions in the visible region correspond with the signal found in the UV-Vis spectrum at around 397 nm. Here, the largest excitation can be ascribed to a ligand-to-ligand charge transfer (LLCT) primarily stemming from a ^{mes}BAP phosphorous centered HOMO-3 molecular orbital to the LUMO+2 orbital that contains the majority of the contributions from ^{mes}BAP with minor contributions from the Gd^{III} center.

Similarly, most of the transitions that correspond to the absorbance peak in the visible region originate from the HOMO-2 orbital which is mainly ^{mes}BAP based with the main contribution arising from the phosphorous atomic orbitals. These excite into LUMO, LUMO+1, LUMO+2, and LUMO+3 orbitals that are primarily ^{mes}BAP-based with small Gd^{III} contributions. The next most intense transition coincides with an absorption around 308 nm (3.24×10^4 cm^{-1}). This exhibits excitations from a primarily ^{mes}BAP based HOMO-1 to LUMO+4 and LUMO+5 that contain considerable contributions from ^{mes}BAP and the Gd^{III} centers. The HOMO and LUMO orbitals are illustrated in Figure 6 with their absolute energies attained from broken symmetry orbitals. Further information regarding the frontier orbitals involved in electronic excitations of the UV-Vis region are given in Table S2 alongside their depictions.

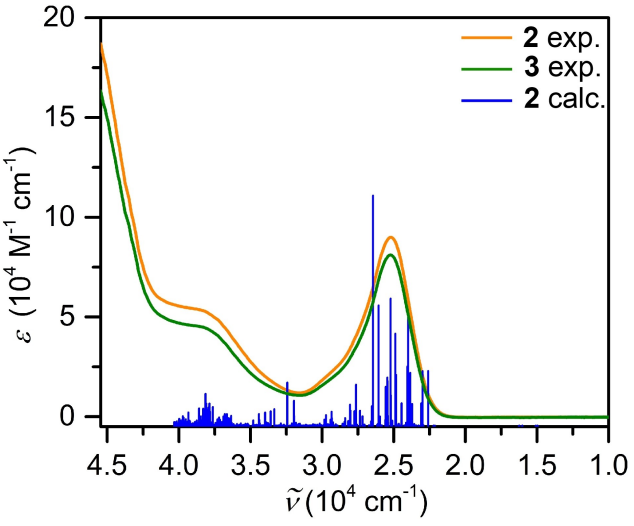

Figure 3. UV-Vis absorption spectra recorded from 220–1000 nm in THF solutions of [{^{mes}BAP}$_2$Gd(THF)(μ-Cl)]$_2$, **2** (orange line) at 10 μM concentration, and [{^{mes}BAP}$_2$Dy(THF)(μ-Cl)]$_2$, **3** (green line) at 10 μM concentration. The calculated electronic transitions are depicted as blue lines.

Magnetic Measurements

The magnetic properties of **2** and **3** were probed under static magnetic fields. DC magnetic susceptibility data ($\chi_M T$) were collected from 2–300 K under 0.1, 0.5, and 1.0 T dc fields, Figures S22, S23, S26 and S27. The room temperature $\chi_M T$ values for **2** and **3** under a dc field of 0.1 T are 16.44 cm^3 K mol^{-1} and 28.77 cm^3 K mol^{-1}, respectively, which are in good accordance with the expected values for two non-interacting Gd^{III} ions (15.76 cm^3 K mol^{-1}) and Dy^{III} ions (28.34 cm^3 K mol^{-1}).[38] For **3**, as the temperatures were lowered, a gradual decrease of $\chi_M T$ values is observed, Figure 4, consistent with thermal depopulation of excited spin states as the thermal energy is reduced. For **2**, upon lowering the temperature, the $\chi_M T$ values remain approximately constant until 13 K, followed by a more significant drop in $\chi_M T$.

The f^7 isotropic configuration of Gd^{III} allows for the quantification of the magnetic exchange coupling between the Gd^{III} centers of **2** by simulating the experimental dc magnetic

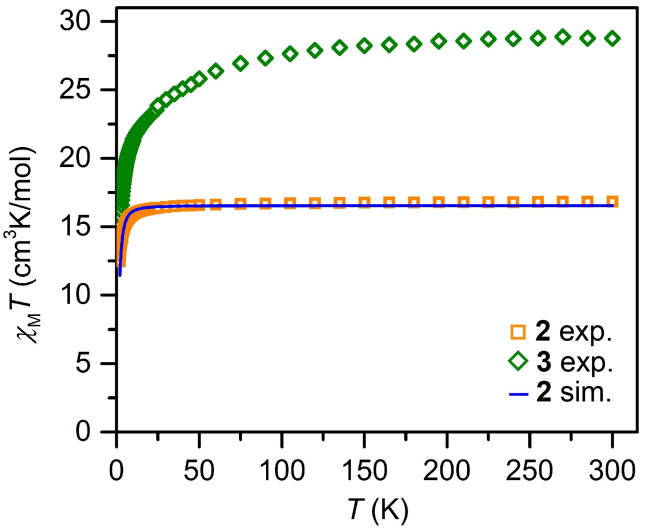

Figure 4. Variable-temperature dc magnetic susceptibility data for restrained polycrystalline samples of [{^{mes}BAP}$_2$Gd(THF)(μ-Cl)]$_2$, **2** (orange squares), and [{^{mes}BAP}$_2$Dy(THF)(μ-Cl)]$_2$, **3** (green diamonds) collected under a 0.1 T applied dc field from 2 K to 300 K. The blue solid line corresponds to a simulated fit (with fit parameters being $J = -0.0035 \pm 0.0013$ cm^{-1} and $g = 2.0497 \pm 0.0023$).

susceptibility data under use of the program PHI.[39] The determination of the magnitude of the exchange coupling constant was carried out using the $\widehat{H} = -2J\widehat{S}_{Gd1}\widehat{S}_{Gd2}$ spin-only Hamiltonian. Here, J represents the exchange coupling constant for the two Gd^{III} centers and the $\widehat{S}$ terms are the spin operators for each Gd^{III} ion. The simulation of the experimental data collected under a 0.1 T dc field yielded $J = -0.0035 \pm 0.0013$ cm^{-1} and $g = 2.0497 \pm 0.0023$. This g-value suggests a minimal perturbation from that of a free Gd^{III} ion.[40] Furthermore, the magnitude of the J value alludes to a weak magnetic exchange interaction between the metal centers. Since Gd^{III} is innate to contracted 4*f* orbitals, the general expectation for the coupling in a dinuclear gadolinium complex where the two metal centers are bridged through diamagnetic ligands such as halides, as is the case in **2**, to be weak if present at all. Thus, our experimental results are in line with the expectation based on electronic structure considerations.

The field-dependent magnetization data of **2** and **3** feature a rapid increase at 2 K to 15.41 $N\mu_B$ and 11.48 $N\mu_B$, respectively, Figures S24 and S28. The reduced magnetization data for **2** exhibit superimposable curves, indicative of the isotropic nature of the Gd^{III} ions, Figure S25. By contrast, the reduced magnetization data for **3** show non-superimposable curves, suggestive of the substantially anisotropic nature of the Dy^{III} ions, Figure S29.

The Kramers ion electron configuration (f^9) innate to Dy^{III} paired with its enormous magnetic anisotropy originating from large unquenched orbital momentum and spin-orbit coupling, renders it an attractive candidate for single-molecule magnet (SMM) design.[41,42] The construction of powerful multinuclear SMMs hinges on both the orientation of the magnetic axis for each metal center (in case of Dy, axiality is optimal) and the strength of magnetic exchange. To probe whether **3** could exhibit slow magnetic relaxation, ac magnetic susceptibility measurements were conducted under applied dc fields of 0, 1000 and 3000 Oe. Under any field, out-of-phase signals were absent suggesting a lack of SMM behavior in complex **3**. In addition, the field-dependent magnetization hysteresis loop remains superimposable at the lowest experimental temperature of 1.8 K revealing the absence of any SMM behavior, Figure S30. The lack of SMM behavior may be traced to strong transverse anisotropic fields introduced by the equatorially coordinating phosphide and THF molecules, counteracting the single-ion magnetic anisotropy of the Dy^{III} ions.

Computational Studies

The half-filled *f*-electron valence shell and isotropic nature of the Gd^{III} ion facilitates an evaluation of the electronic structure of **2** with Density Functional Theory (DFT) calculations. To predict the strength of magnetic coupling between the two Gd^{III} centers, the spin density of one of the Gd^{III} centers was flipped using the 'flipspin' functionality of ORCA, Figure 5.[43] The magnetic exchange coupling constant (J) was calculated following the approach $J = -(E_{HS} - E_{BS})/(\langle S^2\rangle_{HS} - \langle S^2\rangle_{BS})$ where E_{HS} and E_{BS} represent the energies of the high spin and the broken symmetry states, respectively, and $\langle S^2\rangle_{HS}$ and $\langle S^2\rangle_{BS}$ are the total spin angular momenta for the high spin and broken symmetry states.[44] This method predicts a weak antiferromagnetic exchange coupling constant of -0.03 cm^{-1}, which is in agreement with the experimentally derived small antiferromagnetic exchange coupling constant of $J =$

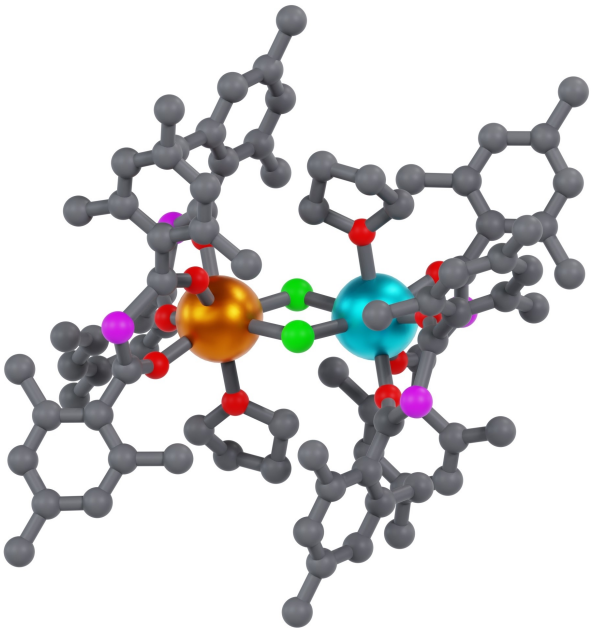

Figure 5. Spin density depiction generated from broken symmetry DFT calculations on the geometry optimized structure of [{^{mes}BAP}$_2$Gd(THF)(μ-Cl)]$_2$, **2**. Larger orange and teal spheres represent the different phases of spin density, exhibiting the spin flip. Smaller red, pink, green, and gray spheres constitute O, P, Cl, and C atoms, respectively. H atoms have been omitted for clarity.

-0.0035 cm^{-1}. This calculation was carried out on unoptimized crystal coordinates to better mimic experimental measurement conditions.

Crystal coordinates of **2** were optimized using the uTPSSh functional prior to subsequent computational calculations. Optimized coordinates and the absolute energy of the structure are provided in Table S3. For the TD-DFT calculations, Zeroth Order Regular Approximation (ZORA) to the Dirac equation was incorporated to take into account the relativistic effects. HOMO and LUMO orbitals, participating in electronic transitions, are depicted in Figure 6.

Conclusion and Outlook

The first dinuclear trivalent rare earth complexes bearing ^{mes}BAP ligands, [{^{mes}BAP}$_2$RE(THF)(μ-Cl)]$_2$ (RE=Y (**1**), Gd (**2**) and Dy (**3**)), were synthesized and unequivocally characterized using experimental and computational methods. Crystallographic and NMR studies indicate an asymmetric coordination of the ^{mes}BAP ligands onto the RE metals centers. **2** exhibits weak antiferromagnetic coupling ($J = -0.0035 \pm 0.0013$ cm^{-1}) between the RE^{III} centers which was confirmed through broken symmetry DFT computations. The similar trend in the dc magnetic susceptibility data for **3** suggests also that there is a weak antiferromagnetic coupling present. All three compounds primarily show electronic excitations in the UV region and high energy visible region, corroborating with the computationally generated electronic transitions. The crystal field comprised of the coordinated THF molecules, and the positioning of the BAP ligands may distort the magnetic axis and anisotropy of each RE^{III} center, precluding single-molecule magnet behavior.

The presented new class of compounds may demonstrate viable starting materials for the synthesis of inorganic and organic ligand bridged multinuclear systems that may be achieved through insertion or salt elimination reactions. This set of compounds may also be attractive candidates for the activation of small molecules under reducing conditions. In fact, the ^{mes}BAP ligand is redox-inactive and hence, able to stabilize *f*-elements in various oxidation states. In addition, the nature of the R group of the acyl {RCO} units in BAP ligands can be fine-tuned which may allow access to complexes with differing metal coordination numbers. The ability of the ligand to bind through the phosphorous and oxygen atoms, may provide an

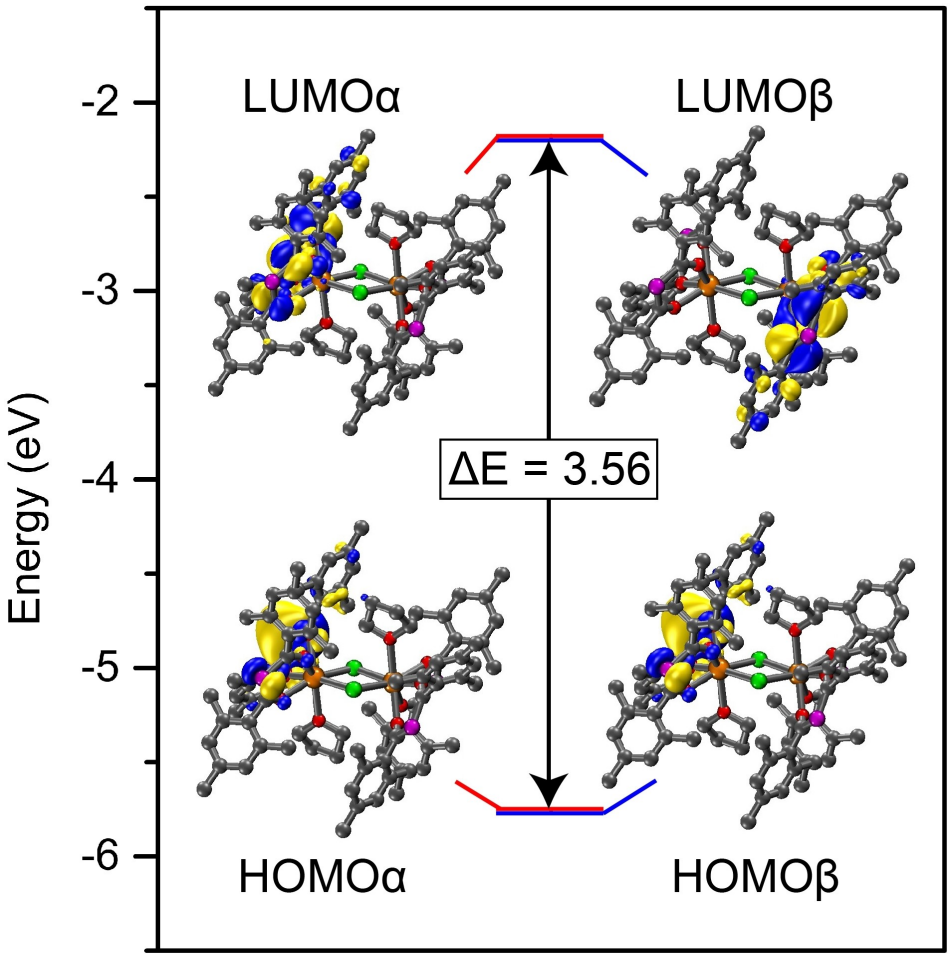

Figure 6. Energy diagram depicting α and β manifolds of the highest occupied molecular orbital (HOMO) and the lowest unoccupied molecular orbital (LUMO) of [{^{mes}BAP}$_2$Gd(THF)(μ-Cl)]$_2$, **2**. Orange, red, pink, green, and gray spheres represent Gd, O, P, Cl, and C atoms. Blue and yellow surfaces illustrate the distribution of the molecular orbitals. Iso values for all surfaces are set to 0.03.

additional layer of accessible synthetic scope such as the pursuit of hetero-multinuclear coordination complex formation via different binding moieties.

Experimental Section

General Information

All manipulations were performed under an inert N_2 atmosphere with exclusion of oxygen and moisture using glovebox and Schlenk techniques unless mentioned otherwise. House N_2 gas was purified using a MBraun HP-500-MO-OX gas purifier before use. Tetrahydrofuran (THF) and toluene were dried and purified by refluxing over Na–K alloy and K metal, respectively, prior to distillation. *n*-Hexane was dried by refluxing over calcium hydride and distilled prior to use. The absence of water and oxygen was confirmed by testing all dried solvents with a drop of potassium benzophenone radical solution in the glovebox. Anhydrous YCl_3, $GdCl_3$, and $DyCl_3$ were purchased from Sigma-Aldrich and were used without further purification. Potassium bis(trimethylsilyl)amide was purchased from Sigma-Aldrich and was recrystallized from toluene prior to use. Bis(mesitoyl)phosphine was prepared according to literature methods.[45] UV-Vis spectroscopic data were collected on an Agilent Cary60 spectrophotometer using a 1 cm path length cuvette fitted with a Schlenk adapter. IR spectra were obtained from a Cary 630 diamond ATR-IR spectrometer under an inert N_2 atmosphere. A PerkinElmer 2400 Series II CHNS/O analyzer was used for CHN elemental analyses.

Synthesis of K(^{mes}BAP)

K(^{mes}BAP) was synthesized through a modified literature procedure.[21] 597.0 mg (1.83 mmol) of bis(mesitoyl)phosphine was completely dissolved in 8 mL of toluene in a 20 mL scintillation vial charged with a magnetic stir bar. To this solution, 364.9 mg (1.83 mmol) of potassium bis(trimethylsilyl)amide was added that was prior dissolved in 6 ml of toluene. The reaction mixture was stirred for 10 minutes at room temperature followed by centrifuging to obtain a bright yellow solid which was subsequently washed twice with 6 mL of toluene and once with 5 mL of hexane. The solid was dried under vacuum to remove any remaining volatile solvents for two hours to afford a bright yellow powder in 88% (585.0 mg) yield.

Synthesis of [{^{mes}BAP}$_2$Y(THF)(μ-Cl)]$_2$, 1

51.6 mg (0.26 mmol) of YCl_3 was suspended in 4 mL of THF in a 20 mL scintillation vial charged with a magnetic stir bar. To this stirring mixture, 192.5 mg (0.52 mmol) of K(^{mes}BAP) was added that was prior dissolved in 3 mL of THF. The reaction mixture was allowed to stir at room temperature for 2 hours before centrifuging to remove the formed byproduct KCl as a colorless solid. The supernatant was filtered through a celite plug into another 20 mL scintillation vial and the solvent was removed under reduced pressure to attain a bright yellow powder (crude yield: 83%). The yellow solid was dissolved in 2 mL of toluene at 60 °C and filtered hot through a Celite plug. From a concentrated toluene solution, stored at −35 °C for two days, yellow plate-shaped crystals of **1** suitable for single crystal X-ray diffraction analysis were obtained in 51% (113.3 mg) crystalline yield. ^{1}H NMR (500 MHz, THF-d_8, 25 °C) δ (ppm): 1.77 (m, 4 H, $OC_2H_4C_2\underline{H_4}$), 2.13 (s, 27 H, $C_6H_2\underline{Me_3}$), 2.22 (s, 27 H, $C_6H_2\underline{Me_3}$), 2.24 (s, 18 H, $C_6H_2\underline{Me_3}$), 3.62 (m, 4 H, $OC_2\underline{H_4}C_2H_4$), 6.72 (s, 16 H, $C_6\underline{H_2}Me_3$); ^{13}C NMR (126 MHz, THF-d_8, 25 °C) δ (ppm): 20.3, 20.31, 21.21 (s, $C_6H_2\underline{Me_3}$), 126.21 (s, $\underline{C_6}H_2Me_3$), 129.02 (s, $\underline{C_6}H_2Me_3$), 129.84 (s, $\underline{C_6}H_2Me_3$), 134.49 (s, $\underline{C_6}H_2Me_3$), 138.38 (s, $(C_6H_2Me_3\underline{C}O)_2P$); ^{31}P NMR (202 MHz, THF-d_8, 25 °C) δ (ppm): 100.31, 100.72 (s, $(C_6H_2Me_3CO)_2\underline{P}$); IR (ATR, cm^{-1}) 2914 (br), 2320 (w), 1607 (m), 1505 (vs), 1338 (s), 1205 (s), 886 (vs), 725 (m). Anal. Calcd for $C_{88}H_{104}Cl_2Y_2O_{10}P_4$•2 C_7H_8: C 65.21, H 6.44, N 0.00. Found: C 64.78, H 6.76, N 0.05. Note: Following crystallization from toluene, the solubility of **1** significantly increased, rendering **1** partially soluble in hexane. This phenomenon may be attributed to enhanced solubility originating from four co-crystallized toluene molecules within the unit cell. As a result, the crystalline yield is lower than the crude yield. The same solubility behavior, affecting yields, is observed for **2** and **3**, respectively (see below).

Synthesis of [{^{mes}BAP}$_2$Gd(THF)(μ-Cl)]$_2$, 2

Following the synthetic procedure for **1**, **2** was obtained as a yellow powder (crude yield: 75%). From a concentrated toluene solution at −35 °C for two days, yellow-orange plate-shaped crystals of **2** suitable for single crystal X-ray diffraction analysis were obtained in 52% (203.3 mg) crystalline yield. Weights used: 112.5 mg (0.43 mmol) of $GdCl_3$, 311.3 mg (0.85 mmol) of K(^{mes}BAP). IR (ATR, cm^{-1}) 2914 (br), 2731 (w), 2320 (w), 1608 (m), 1500 (vs), 1376 (s), 1205 (s), 1021 (m), 845 (vs), 729 (m); Anal. Calcd for $C_{88}H_{104}Cl_2Gd_2O_{10}P_4$: C 57.72, H 5.73, N 0.00. Found: C 57.36, H 5.74, N 0.03.

Synthesis of [{^{mes}BAP}$_2$Dy(THF)(μ-Cl)]$_2$, 3

Following the synthetic procedure for **1**, **3** was obtained as yellow powder (crude yield: 78%). From a concentrated toluene solution at −35 °C for two days, yellow-orange plate-shaped crystals of **3** suitable for single crystal X-ray diffraction analysis were obtained in 44% (152.0 mg) crystalline yield. Weights used: 100.9 mg (0.38 mmol) of $DyCl_3$, 273.7 mg (0.75 mmol) of K(^{mes}BAP). ^{31}P NMR (202 MHz, THF-d_8, 25 °C) δ (ppm): 91.57 (s, $(C_6H_2Me_3CO)_2\underline{P}$); IR (ATR, cm^{-1}) 2914 (br), 2731 (w), 2321 (w), 1608 (m), 1501 (vs), 1374 (s), 1205 (s), 845 (vs), 726 (m); Anal. Calcd for $C_{88}H_{104}Cl_2Dy_2O_{10}P_4$: C 57.39, H 5.69, N 0.00. Found: C 57.49, H 5.67, N 0.03.

Magnetic Measurements

All magnetic data were collected on a Quantum Design MPMS3 SQUID magnetometer. Sample preparation was carried out under an inert Ar atmosphere with eicosane as a diamagnetic matrix for immobilization of polycrystalline samples. 21.1 mg and 19.9 mg of **2** and **3**, respectively, were used for preparing the samples that were sealed airtight, transferred and mounted onto the sample holder of the SQUID instrument. DC magnetic susceptibility data were collected from 2 K–300 K temperature range. All data were corrected considering diamagnetic contributions from eicosane and core diamagnetism using Pascal's constants.[46]

X-ray Crystallography

Crystallographic data was collected on an XtaLAB Synergy, Dualflex and HyPix diffractometer under Cu Kα radiation. Yellow plate-shaped crystals of **1** and yellow-orange plate-shaped crystals of **2** and **3** with dimensions of 0.20×0.14×0.04 mm^3, 0.14×0.098×0.043 mm^3 and 0.179×0.125×0.044 mm^3, respectively, were suspended in *n*-paratone oil prior to mounting on a nylon loop. Temperature during data collection was accomplished at 100.0(1) K using an Oxford Cryosystems low-temperature device.

For all three compounds, data collection strategy, unit cell determination and data reduction were performed with corrections for Lorentz polarization by the CrysAlisPro software.[47] A numerical absorption correction based on Gaussian integration over a multi-faceted crystal model utilizing spherical harmonics implemented in the SCALE3 ABSPACK scaling algorithm[48] was utilized to account for absorption effects. Structures of **1** and **2** were solved in the space group $P2_1/c$, whereas **3** was solved in the space group $P\bar{1}$. For solving, dual methods with *ShelXT*[49] was employed and refined by least squares using version 2019/2 of *XL*[50] integrated into Olex2.[51] All non-H atoms were refined anisotropically, while H atom positions were generated geometrically and refined using the riding model.

Computational Methods

Density functional theory calculations were carried out for **2** using ORCA 5.0.3 software.[43,52] Geometry optimization of **2** was performed using uTPSSh functional[53,54] with D3BJ dispersion correction[55,56] at def2-TZVP level.[57,58] TD-DFT calculations were conducted on the optimized structure of **2** with a CPCM THF solvent model[59] using uB3LYP functional[60,61] and ZORA relativistic treatment for 500 excited states.[62] ZORA-def2-TZVPP basis set was applied for treating O, Cl, and P atoms, whereas SARC2-ZORA-QZVP basis set was used in the treatment of Gd atoms. All calculations employed the SARC/J auxiliary basis set.[62,63] Generation of spin densities and molecular orbitals was accomplished using the orca_plot module and the VMD program[64] was employed for visualizations. Electronic transitions calculated through TD-DFT were shifted by 0.3 eV to coincide better with experimental data.

Supporting Information Summary

Computational data, magnetic data, spectroscopic data, and detailed crystallographic information for **1**, **2**, and **3** are located in the Supporting Information. Deposition Numbers 2352360 (for **1**), 2352361 (for **2**), 2352362 (for **3**) contain the supplementary crystallographic data for this paper. These data are provided free of charge by the joint Cambridge Crystallographic Data Centre and Fachinformationszentrum Karlsruhe Access Structures service.

Acknowledgements

This work was funded in part through the National Science Foundation (NSF) Faculty Early Career Development Program (CAREER) through grant no. CHE-2339595. We are thankful to Dr. Richard Staples (MSU) for assistance with single-crystal X-ray diffraction measurements. We would like to extend our special thanks to Prof. Dr. Hansjörg Grützmacher from ETH Zurich for the generous supply of chemicals. The computational analyses were supported through resources and services provided by the Institute for Cyber-Enabled Research at MSU. The single-crystal X-ray diffractometer was funded by the MRI program of the National Science Foundation under grant no. CHE-1919565.

Conflict of Interests

The authors declare no conflict of interest.

Data Availability Statement

The data that support the findings of this study are available in the supplementary material of this article.

Keywords: Rare earth metal · Phosphides · Magnetic coupling · Density functional theory · Spectroscopy

[1] J. D. Rinehart, J. R. Long, *Chem. Sci.* **2011**, *2*, 2078.
[2] P. M. Zeimentz, S. Arndt, B. R. Elvidge, J. Okuda, *Chem. Rev.* **2006**, *106*, 2404–2433.
[3] S. A. Cotton, *Lanthanide and Actinide Chemistry*, Wiley, Chichester, England, Hoboken, NJ **2006**.
[4] W. J. Evans, C. A. Seibel, J. W. Ziller, *J. Am. Chem. Soc.* **1998**, *120*, 6745–6752.
[5] M. Tricoire, N. Mahieu, T. Simler, G. Nocton, *Chem. Eur. J.* **2021**, *27*, 6860–6879.
[6] S. Schäfer, S. Kaufmann, E. S. Rösch, P. W. Roesky, *Chem. Soc. Rev.* **2023**, *52*, 4006–4045.
[7] A. Døssing, *Eur. J. Inorg. Chem.* **2005**, *2005*, 1425–1434.
[8] J.-C. G. Bünzli, *Coord. Chem. Rev.* **2015**, *293–294*, 19–47.
[9] S. Demir, M. I. Gonzalez, L. E. Darago, W. J. Evans, J. R. Long, *Nat. Commun.* **2017**, *8*, 2144.
[10] M. A. AlDamen, J. M. Clemente-Juan, E. Coronado, C. Martí-Gastaldo, A. Gaita-Ariño, *J. Am. Chem. Soc.* **2008**, *130*, 8874–8875.
[11] P. Zhang, F. Benner, N. F. Chilton, S. Demir, *Chem* **2022**, *8*, 717–730.
[12] D. Mara, F. Artizzu, B. Laforce, L. Vincze, K. Van Hecke, R. Van Deun, A. M. Kaczmarek, *J. Lumin.* **2019**, *213*, 343–355.
[13] A. P. Bassett, S. W. Magennis, P. B. Glover, D. J. Lewis, N. Spencer, S. Parsons, R. M. Williams, L. De Cola, Z. Pikramenou, *J. Am. Chem. Soc.* **2004**, *126*, 9413–9424.
[14] M. Hasegawa, A. Nakao, M. Masui, T. Tamura, D. Suzuki, W. Linert, Y. Fukuda, T. Hoshi, *Chem. Phys.* **2001**, *269*, 323–337.
[15] D. I. Alexandropoulos, K. A. Schulte, K. R. Vignesh, K. R. Dunbar, *Chem. Commun.* **2018**, *54*, 10136–10139.
[16] M. Vonci, C. Boskovic, *Aust. J. Chem.* **2014**, *67*, 1542.
[17] C. Boskovic, *Acc. Chem. Res.* **2017**, *50*, 2205–2214.
[18] L. Weber, K. Reizig, R. Boese, *Organometallics* **1985**, *4*, 1890–1891.
[19] M. Madadi, B. Khalili Najafabadi, M. A. Fard, J. F. Corrigan, *Eur. J. Inorg. Chem.* **2015**, *2015*, 3094–3101.
[20] D. W. Meek, T. J. Mazanec, *Acc. Chem. Res.* **1981**, *14*, 266–274.
[21] R. Conti, A. Widera, G. Müller, C. Fekete, D. Thöny, F. Eiler, Z. Benkő, H. Grützmacher, *Chem. Eur. J.* **2023**, *29*, e202202563.
[22] J. Hochholzer, P. Waldschmidt, F. W. Heinemann, H. Grützmacher, K. Meyer, *Eur. J. Inorg. Chem.* **2024**, *27*, e202300592.
[23] S. H. Carpenter, N. J. Wolford, B. S. Billow, T. V. Fetrow, N. Cajiao, A. Radović, M. T. Janicke, M. L. Neidig, A. M. Tondreau, *Inorg. Chem.* **2022**, *61*, 12508–12517.
[24] J. Chen, S. H. Carpenter, T. V. Fetrow, J. Mengell, M. L. Kirk, A. M. Tondreau, *Inorg. Chem.* **2022**, *61*, 18466–18475.
[25] S. H. Carpenter, J. Mengell, J. Chen, M. R. Jones, M. L. Kirk, A. M. Tondreau, *Inorg. Chem.* **2024**, *63*, 8516–8520.
[26] H. Asaba, T. Iwasaki, M. Hatazawa, J. Deng, H. Nagae, K. Mashima, K. Nozaki, *Inorg. Chem.* **2020**, *59*, 7928–7933.
[27] H. Sheng, R. Zeng, W. Wang, S. Luo, Y. Feng, J. Liu, W. Chen, M. Zhu, Q. Guo, *Adv. Synth. Catal.* **2017**, *359*, 302–313.
[28] S. Gambarotta, J. Scott, *Angew. Chem. Int. Ed.* **2004**, *43*, 5298–5308.
[29] J. F. Berry, C. M. Thomas, *Dalton Trans.* **2017**, *46*, 5472–5473.
[30] F. Delano IV, S. Demir, *Eur. J. Inorg. Chem.* **2024**, *27*, e202300797.
[31] M. A. Lutoshkin, A. I. Petrov, Y. N. Malyar, A. S. Kazachenko, *Inorg. Chem.* **2021**, *60*, 3291–3304.
[32] F. Delano, S. Deshapriya, S. Demir, *Polyhedron* **2024**, *249*, 116785.
[33] P. Jin, K. Yu, Y. Zhai, Q. Luo, Y. Wang, X. Zhang, Y. Lv, Y. Zheng, *Chin. J. Chem.* **2021**, *39*, 1635–1640.
[34] Z. Lu, G. P. A. Yap, D. S. Richeson, *Organometallics* **2001**, *20*, 706–712.

[35] D. M. Roitershtein, L. N. Puntus, A. A. Vinogradov, K. A. Lyssenko, M. E. Minyaev, M. D. Dobrokhodov, I. V. Taidakov, E. A. Varaksina, A. V. Churakov, I. E. Nifant'ev, *Inorg. Chem.* **2018**, *57*, 10199–10213.
[36] G. Glockler, *J. Phys. Chem.* **1958**, *62*, 1049–1054.
[37] S. Aime, L. Barbero, M. Botta, *Magn. Reson. Imaging* **1991**, *9*, 843–847.
[38] H. L. C. Feltham, S. Brooker, *Coord. Chem. Rev.* **2014**, *276*, 1–33.
[39] N. F. Chilton, R. P. Anderson, L. D. Turner, A. Soncini, K. S. Murray, *J. Comput. Chem.* **2013**, *34*, 1164–1175.
[40] A. Borel, E. Tóth, L. Helm, A. Jánossy, A. E. Merbach, *Phys. Chem. Chem. Phys.* **2000**, *2*, 1311–1317.
[41] S. Demir, J. M. Zadrozny, J. R. Long, *Chem. Eur. J.* **2014**, *20*, 9524–9529.
[42] E. M. Fatila, M. Rouzières, M. C. Jennings, A. J. Lough, R. Clérac, K. E. Preuss, *J. Am. Chem. Soc.* **2013**, *135*, 9596–9599.
[43] F. Neese, *WIREs Comput. Mol. Sci.* **2022**, *12*, DOI 10.1002/wcms.1606.
[44] T. Soda, Y. Kitagawa, T. Onishi, Y. Takano, Y. Shigeta, H. Nagao, Y. Yoshioka, K. Yamaguchi, *Chem. Phys. Let.* **2000**, *319*, 223–230.
[45] G. Becker, W. Becker, M. Schmidt, W. Schwarz, M. Westerhausen, *Zeitschrift anorg allge chemie* **1991**, *605*, 7–23.
[46] G. A. Bain, J. F. Berry, *J. Chem. Educ.* **2008**, *85*, 532.
[47] Agilent (2014).CrysAlis PRO. Agilent Technologies Ltd, Yarnton, Oxfordshire, England.
[48] CrysAlisPro, Agilent Technologies, Version 1.171.35.11. Multi-scans absorption correction with SCALE3 ABSPACK scaling algorithm.
[49] G. M. Sheldrick, *Acta. Crystallogr. A. Found. Adv.* **2015**, *71*, 3–8.
[50] G. M. Sheldrick, *Acta Crystallogr. C. Struct Chem.* **2015**, *71*, 3–8.
[51] O. V. Dolomanov, L. J. Bourhis, R. J. Gildea, J. A. K. Howard, H. Puschmann, *J. Appl. Crystallogr.* **2009**, *42*, 339–341.
[52] F. Neese, *WIREs Comput. Mol. Sci.* **2012**, *2*, 73–78.
[53] V. N. Staroverov, G. E. Scuseria, J. Tao, J. P. Perdew, *J. Chem. Phys.* **2003**, *119*, 12129–12137.
[54] V. N. Staroverov, G. E. Scuseria, J. Tao, J. P. Perdew, *J. Chem. Phys.* **2004**, *121*, 11507.
[55] S. Grimme, J. Antony, S. Ehrlich, H. Krieg, *J. Chem. Phys.* **2010**, *132*, 154104.
[56] S. Grimme, S. Ehrlich, L. Goerigk, *J. Comput. Chem.* **2011**, *32*, 1456–1465.
[57] K. A. Peterson, D. Figgen, M. Dolg, H. Stoll, *J. Chem. Phys.* **2007**, *126*, 124101.
[58] F. Weigend, R. Ahlrichs, *Phys. Chem. Chem. Phys.* **2005**, *7*, 3297.
[59] V. Barone, M. Cossi, *J. Phys. Chem. A* **1998**, *102*, 1995–2001.
[60] P. J. Stephens, F. J. Devlin, C. F. Chabalowski, M. J. Frisch, *J. Phys. Chem.* **1994**, *98*, 11623–11627.
[61] A. D. Becke, *J. Chem. Phys.* **1992**, *96*, 2155–2160.
[62] D. A. Pantazis, F. Neese, *J. Chem. Theory Comput.* **2009**, *5*, 2229–2238.
[63] F. Weigend, *Phys. Chem. Chem. Phys.* **2006**, *8*, 1057.
[64] W. Humphrey, A. Dalke, K. Schulten, *J. Mol. Graphics* **1996**, *14*, 33–38.

Manuscript received: May 1, 2024
Revised manuscript received: June 27, 2024
Accepted manuscript online: July 3, 2024
Version of record online: August 21, 2024